An interpretive model for the double peaks of divertor tungsten erosion during type-I ELMs in EAST

Guoliang Xu[1,2,3], Rui Ding[4*], Fang Ding[4], Xiahua Chen[4], Xinyuan Qian[1,2,3], Sebastijan Brezinsek[5], Xiang Gao[1,2,3], Qing Zang[1,2,3], Liang Wang[4], Yinxian Jie[1,2,3], Peiguang Yan[1], Junling Chen[4], Jiangang Li[1,2,3], Yuanxi Wan[1,2,3]

[1]College of Physics and Optoelectronic Engineering, Shenzhen University, Shenzhen 518060, China

[2]Key Laboratory of Optoelectronic Devices and Systems of Ministry of Education and Guangdong Province, College of Physics and Optoelectronic Engineering, Shenzhen University, Shenzhen 518060, China

[3]Advanced Energy Research Center, Shenzhen University, Shenzhen 518060, China

[4]Institute of Plasma Physics, Chinese Academy of Sciences, Hefei 230031, China

[5]Forschungszentrum Jülich GmbH, Institut für Energie- und Klimaforschung - Plasmaphysik, Partner of the Trilateral Euregio Cluster (TEC), 52425 Jülich, Germany

* Corresponding author, E-mail: rding@ipp.ac.cn

Abstract:

Double peaks of divertor tungsten erosion during type-I edge-localized modes (ELMs) were observed in the EAST tokamak. To study this unique phenomenon, an analytic model of plasma expansion into vacuum is used to investigate the ELM parallel transport along the magnetic field line to the divertor target. Modeling results reveal that during ELM bursts, the energetic C^{6+} transport is slower than the main ions due to a lower initial thermal speed. The time of C^{6+} arriving at the divertor target from the modeling is consistent with the second tungsten erosion peak. Based on the particle flux from the transport model, a newly developed mixed-material model quantitively reproduced the intra-ELM tungsten erosion profiles for both deuterium and helium discharges. A lithium-carbon coating makes the heavier impurity (C^{6+}) comparatively more effective than the main ions on tungsten sputtering, and thus makes the second tungsten erosion peak more remarkable on EAST experiments.

Key words: plasma material interaction, tungsten erosion, ELM, EAST, double peaks

1. Introduction:

Tungsten has been widely used as the plasma-facing material (PFM) in current tokamak devices, and is also foreseen for the future fusion reactors. Erosion of tungsten PFM is a critical issue, which can not only limit the material lifetime, but also lead to tungsten impurity degrading the plasma performance. Previous studies show that at steady state tungsten erosion is mainly due to physical sputtering by incident impurity ions [1-5]. During transient events such as edge-localized modes (ELMs), tungsten erosion by the main ion species become more important because of the high incident energy. The intra-ELM tungsten erosion rate is normally much higher than the inter-ELM erosion rate

[6]. The physics process of ELM-induced tungsten erosion is also much more complicated and validated modeling is essential.

During ELM bursts, energetic particles are transported from the hot pedestal region to the divertor targets. Previous studies on JET and DIII-D show that the intra-ELM tungsten erosion rate is associated with electron temperature and impurity concentration at the pedestal top [7-11]. Therefore, it is necessary to model the ELM transport processes before studying the intra-ELM divertor tungsten erosion. Since kinetic simulation of ELM transport is complicated and time consuming, two simple analytic models were developed recently to describe the parallel transport of ELMs in the scrape-off layer (SOL). One is the free-streaming transport model (FSM) [12, 13], which solves the Vlasov equation in the absence of Coulomb potential. In this model, the initially Maxwellian distributed plasma bunch is considered to transport freely to the divertor at an average speed of the ion thermal speed. The free-streaming model has been proved to capture the main features of the ELMs, and the free-streaming equations successfully reproduced the particle and energy flux density on the divertor of JET and ASDEX-Upgrade [14]. Another model is derived by solving the Vlasov equation for both electrons and ions to describe the free expansion process of a plasma bunch into a vacuum [15, 16]. With a quasi-neutral approximation, the self-consistent Coulomb potential is also considered in this free expansion model (FEM). The model was firstly used in the field of laser-driven thermonuclear fusion, and then applied to describe the parallel ELM transport by Moulton in [17]. The analytic solution is proved to be a generalized version of the free-streaming model for plasma expansion and validated by large amount of experimental data on JET [9, 10, 17].

For fusion devices with multiple PFMs, a mixed-material environment is unavoidable. Previous DIII-D experimental and modeling results reveal that there exists large amount of deposited carbon on the surface of tungsten samples, and the existence of carbon has a noteworthy influence on the tungsten erosion process for both inter- and intra-ELM phases [4, 7]. Dynamic simulations for ITER tungsten divertor also show that the deposited beryllium on the tungsten surface significantly affects the total tungsten erosion rate [18]. However, the complicated mixed-material condition in EAST leads to a challenge for modeling of tungsten divertor erosion.

This paper covers a unique experimental phenomenon of double erosion peaks for EAST tungsten divertor during type-I ELMs burst and the corresponding modeling explanations. The tungsten erosion processes during type-I ELMs for both deuterium and helium discharges are analyzed. By evaluating the ELM parallel transport and lithium-carbon coating on the divertor, the unique double peaks phenomenon of EAST tungsten erosion is well-explained.

The rest of paper is organized as follows. The experimental setup is described in section 2. The parallel transport processes of main ions and C^{6+} impurities during ELMs are analyzed in section 3. The intra-ELM tungsten erosion is calculated based on a divertor

mixed material model in section 4, followed by discussion and conclusions in section 5.

2. Experimental setup

The EAST tokamak is a D-shaped fully superconducting device with an ITER-like tungsten upper divertor, a graphite lower divertor and the molybdenum first wall. In order to provide references for the ITER helium operation phase, helium experiments were carried out on EAST in 2019. During the helium campaign, type-I ELMy H-modes have been achieved [19], which provides a good platform to investigate the tungsten erosion during ELMs.

The cross section of EAST main chamber and key diagnostics used in this work are shown in figure 1. To monitor the divertor tungsten erosion, a multichannel spectroscopy system with 22 line of sights observing the upper outer divertor region was installed to measure the 400.9 nm WI emission intensity [20]. The time resolution of the W divertor spectroscopy is 10 μs, which is high enough to resolve the ELMs. 13 triple Langmuir probes are located on the upper outer divertor to measure the local electron temperature and the particle flux with a time resolution of 20 μs [21]. The filterscope system with 13 chords monitoring the upper divertor region can provide the Dα (656.1 nm) and HeI (448.1 nm) emission data [22]. Meanwhile, the Thomson scattering system [23] can provide the electron temperature and density at the pedestal region.

Unlike the single peak of intra-ELM W erosion profiles in other machines [11, 24], double peaks of W erosion during some D and He discharges with type-I ELMs were observed on EAST. As shown in figure 2, for a typical deuterium discharge 87448 and a helium discharge 87045, the intra-ELM tungsten erosion rate at the strike point on the upper outer divertor firstly peaks in accordance with the peak of the ion saturation current *Jsat*, then the second higher W erosion peak appears about 1 ms after the peak of *Jsat*. Note that the second peak in the figure 2 means a cluster of peaks (with a large fluctuation) which is obviously higher than the previous peak, and the multiple-ELMs averaged double-peak profiles are provided in figure 5. To study this distinguishing double-peak phenomenon and compare the W erosion contribution from deuterium and helium, two well-diagnosed discharges are selected for intra-ELM W erosion modeling. Since the helium concentration C_{He} of the chosen discharges equals 0 and 0.6 respectively, we name these two discharges as ‘D discharge’ and ‘He discharge’ hereafter. The detail information of the chosen discharges is listed in table 1. In order to make the modeling result more robust, the selected two discharges have different pedestal parameters. Compared to the He discharge, the D discharge has a higher pedestal density and a lower pedestal temperature.

Table 1. Comparison of relevant plasma parameters for intra-ELM W erosion between D and He discharges modeling

shot NO.	C_{He} ($n_{He}/(n_{He}+n_D)$)	n_{e_ped} (m^{-3})	T_{e_ped} (eV)	P_{heat} (MW)	δW (KJ)	$\delta W/W$ (%)	f_{ELM} (Hz)	L (m)	δt (ms)	σ_0 (m)
87448	0	1.2×10^{20}	357	3	18	10	18	452	1.2	28
87045	0.6	3.9×10^{19}	646	5	14	8	80	467	1.1	17

3. Parallel ELM transport simulation

The FEM is employed to describe the one-dimensional transport of EAST type-I ELMs from the outer midplane (OMP) to the strike-point of the outer divertor target. By leveraging the diagnostic data of the pedestal Thompson scattering and divertor target Langmuir probes, uncertain parameters in the FEM can be determined. In the FEM, the parallel particle flux density arriving at the divertor target carried by an ELM is predicted as [17]:

$$\Gamma_{ELM} = \frac{n_{ELM}\, Lc_s^2(t_{ELM}/\sigma_0^2)}{(1+(c_s t_{ELM}/\sigma_0)^2)^{3/2}} e^{\frac{-(L/\sigma_0)^2}{2(1+(c_s t_{ELM}/\sigma_0)^2)}} \quad (1)$$

where n_{ELM} and c_s are the electron density and the ion sound speed at the pedestal top, L is the magnetic connection length between the outer midplane and the divertor target, σ_0 is the initial parallel extent of ELM source, and t_{ELM} is the ELM evolution time starting from the OMP. Therefore, the ion saturation current at the strike point can be expressed as:

$$J_{sat} = \frac{Zen_{ELM}\, Lc_s^2((t+\delta t)/\sigma_0^2)}{(1+(c_s(t+\delta t)/\sigma_0)^2)^{3/2}} e^{\frac{-(L/\sigma_0)^2}{2(1+(c_s(t+\delta t)/\sigma_0)^2)}} + J_{satbg} \quad (2)$$

where Z is the effective charge state of the main ions (Z equals 1 and 1.6 for the D discharge and He discharge respectively), and J_{satbg} is the ion saturation current contributed by the background plasma, which can be measured by the divertor Langmuir probe between ELMs. Note that t is the ELM evolution time starting from the divertor target, and δt is to represent the time difference between ELM start time of OMP and the target, i.e. $t + \delta t = t_{ELM}$. The electron density and the electron temperature at the pedestal top (n_{ELM} and T_{e_ped}) can be obtained from the Thomson scattering diagnostic. Then c_s is expressed as: $c_s = ((ZT_{e\_ped} + T_{i\_ped})/m_i)^{1/2} = ((Z+1)T_{e\_ped}/m_i)^{1/2}$, with $T_{i\_ped} = T_{e\_ped}$ assumed. By setting $L, \delta t$, and σ_0 as fitting parameters, equation (2) can be directly used to fit the intra-ELM ion saturation current measured from the divertor Langmuir probes.

The ELM onset on the divertor is distinguished by the maximum-slope of the D_α (HeI) signal, and the intra-ELM data is chosen within -0.5 ms to 5 ms from the ELM onset. Figure 3 shows the best fitting results of ion saturation current for both D and He discharges. As shown in figure 3, FEM can well reproduce the quick rise and slow decay of divertor particle flux during ELMs. The fitting values of L, δt and σ_0 are listed in table 1. After obtained the value of σ_0, the self-consistent electric field at different locations can be derived [15, 17]:

$$E = \frac{T_{e\_ped} x/\sigma_0^2}{e(1+(c_s t_{ELM}/\sigma_0)^2)^2} \quad (3)$$

where x represents different location along the magnetic field line from the OMP. Due to the exist of the electric field, ions are accelerated while moving to the target.

A one-dimensional Monte Carlo tracing code is developed to simulate the particle transport with electric field. In this code, the electric field changes with x and t_{ELM} according to the equation (3). Deuterium, helium and carbon particles are injected and traced in a region of $-L < x < L$ with the given electric field. The initial injected particles satisfy a Gaussian distribution along x and a Maxwellian velocity distribution with the pedestal electron temperature T_{e_ped}:

$$S_\alpha = \frac{n_{\alpha 0}}{\sqrt{2\pi} v_{T\alpha}} \exp\left(\frac{-x^2}{2\sigma_{\alpha 0}^2}\right) \exp\left(\frac{-v^2}{2v_{T\alpha}^2}\right) \quad (4)$$

where α represents the ion species, i.e. D, He or C. $n_{\alpha 0}$ is the initial peak density which equals to the value at the pedestal top. $v_{T\alpha}$ is the ion thermal speed, $v_{T\alpha} = \sqrt{T_{e\_ped}/m_\alpha}$. $\sigma_{\alpha 0}$ is the initial parallel extent of the source, which is considered to be proportional to $v_{T\alpha}$, and thus can be inferred from the previous fitted σ_0 by $\sigma_{\alpha 0} = \sqrt{m_0/m_\alpha}\,\sigma_0$ with m_0 referring to the average mass of the main ions.

In addition to deuterium and helium, carbon is the most important impurity existing in the plasma and needs to be taken into account. The initial peak density of carbon n_{C0} is taken as 1% of the total ions in the modeling as an example. The injected ions are assumed to be fully ionized due to the high electron temperature at the pedestal top. The ELM transport time is proved to be too short for ions to recombine to a lower charge state [7], and thus the recombination is not considered during the particle transport.

The parallel particle flux density arriving at the divertor target (x=L) from the calculation is shown in figure 4(a) and 4(b). Note that the C^{6+} flux density is multiplied by 100 for a better comparison. For both D and He discharges, the peak of C^{6+} flux density appears obviously later than the main ions due to the lower initial thermal speed. The He discharge has a relatively higher pedestal temperature, thus has a higher average speed. The time difference of the main ions and C^{6+} arriving the divertor target is shorter for the He discharge than that of the D discharge consequently.

After the parallel particle flux density is obtained, the related ion saturation current can be estimated by:

$$J_{sat} = \sum eZ_\alpha \Gamma_\alpha + J_{sat\mathrm{bg}} \quad (5)$$

As shown in figure 3, the J_{sat} estimated from the numerical results matches well with the experimental data, which indicates that the transport process and the existing electric field are self-consistent. Note that the numerical results shown in figure 3 are shifted by a δt due to the different definitions of ELM start time between OMP and the target, and δt equals to 1.2 ms and 1.1 ms for the D and He discharges respectively,

as listed in table 1.

Another important parameter is the impact energy of impinging particles. The parallel velocity of particles arriving at the divertor target can be obtained from the Monte Carlo modeling. As shown in figure 4(c) and 4(d), the velocities of D^+, He^{2+} and C^{6+} which are normalized to their initial thermal speed decay exponentially with the time arriving at the target. During the particles transport, the electric field accelerates the ions to a higher speed, and thus the average velocities of the peak particle flux density is more than 2 times higher than the initial thermal speed for all these three ion species. Then the parallel dynamic energy can be expressed as:

$$E_{\alpha dy//} = (v_\alpha / v_{\alpha th})^2 T_{e\_ped} \tag{6}$$

The impact energy contains two parts: the kinetic energy of the streaming particles and energy gained from the sheath potential:

$$E_\alpha = (E_{\alpha dy//} + T_{i\_ped}) + 3Z_\alpha T_e \tag{7}$$

where α represents D, He or C. $E_{\alpha dy//}$ is the parallel kinetic energy calculated by equation (6). An additional T_{i_ped} is included to represent the conventional ion energy in the perpendicular directions and is assumed to be equal to T_{e_ped} . Z_α is the charge state of the impinging particles, and T_e is the electron temperature at the divertor target, which can be obtained from the Langmuir probes.

4. *Intra-ELM tungsten erosion simulation*

The experimental tungsten gross erosion rate is derived from the 400.9 nm WI spectral line intensity Φ_{WI}:

$$\Gamma_W = \frac{S}{XB}(T_e)\Phi_{WI} \tag{8}$$

where the S/XB is the inverse photon efficiency, and it means the number of ionizations per photon. According to previous experimental data, the S/XB depends on T_e and can be expressed as [25]:

$$\frac{S}{XB}(T_e) = 53.7\left(1 - 1.04\exp\left(-\frac{T_e}{22.1}\right)\right) \tag{9}$$

The experimental data of averaged intra-ELM tungsten gross erosion rate during the D discharge and the He discharge is shown in figure 5, where double peaks of tungsten erosion rate during ELMs are clearly shown.

Since the PFM of lower divertor in EAST is graphite, the eroded carbon can be transported into the plasma and redeposited on the tungsten upper divertor. Meanwhile, lithium coating of the first wall has been used as a routine way of wall conditioning on EAST [26, 27], which is favorable for core plasma performance . The lithium coating on the tungsten divertor makes the mix material effects more complicated.

The SDTRIM.SP code [28] is employed to create a mixed material model for

calculation of the intra-ELM tungsten erosion rates. In the SDTRIM.SP code, the target material composition of different thickness can be predefined before calculating the sputtering yields. Both modeling results and post-mortem material analysis suggest there exists a Li-C enriched layer on EAST plasma facing material [29-31]. Therefore, according to EAST experimental condition, a mixed material tungsten sputtering model is created. The simplified mixed material model contains two regions. The first region is a Li-C coating with an atom fraction of $f_{Li}: f_C = 1:1$, while the second region is the pure tungsten substrate. Furthermore, redeposition of eroded tungsten particles can also be mixed in the Li-C enriched layer. The atom ratio of W to C in the Li-C enriched layer is assumed to be equal to the ratio of their flux density impinging to the divertor target, which is about 0.005 according to previous experimental and modeling results [32, 33]. Hence, the atom fraction in the Li-C enriched layer of the simplified mixed material model is set to be $f_{Li}: f_C: f_W = 1:1:0.005$. The thickness of the Li-C coating is an adjustable parameter in this mixed material tungsten sputtering model.

The parallel particle flux densities of D^+, He^{2+} and C^{6+} calculated by the Monte Carlo ELM transport code are put into the mixed material tungsten sputtering model after multiplied by $\sin\theta$, where $\theta = 1.5°$, is the angle between the magnetic field line and the divertor target. With the full parallel velocity distribution of impinging ions from the Monte Carlo modeling taken into account, the impact energy of D^+, He^{2+}, C^{6+} are calculated from equation (7). By adjusting the thickness of the Li-C enriched layer and C^{6+} fraction in the streaming plasma, the intra-ELM tungsten erosion profiles are well reproduced for both D and He discharges, as shown in figure 5. The thickness of the Li-C enriched layer in the mixed material model is set to be 30 Å, meanwhile, the C^{6+} fractions in the streaming plasma are 1.5% and 3% for the D and He discharges respectively, which is similar to the value of streaming C^{6+} fraction on DIII-D [7].

The contributions from different impinging particles calculated by the mixed material tungsten sputtering model are also shown in figure 5. During ELM burst, due to different transport speeds of the streaming ions, the energetic C^{6+} particles arrive later than the main ions and cause the second tungsten erosion peak. For the He discharge, the tungsten erosion caused by the C^{6+} is comparable with that caused by the main ions, whereas for the D discharge the energetic C^{6+} dominates the tungsten erosion even the C^{6+} fraction in the plasma is lower. Although the peak particle flux density of the D discharge is more than 5 times higher than the He discharge, the tungsten erosion rate caused by the main ions is lower than the He discharge. As shown in figure 5(b), the peak tungsten erosion caused by 60% He^{2+} is more than 15 times higher than that caused by 40% D^+, which indicates that the He is much more effective than D on causing tungsten erosion with Li-C coating.

To further assess the influence of the Li-C coating, the tungsten sputtering yields of a pure tungsten model and the new mixed material model with a specified 30 Å Li-C coating are compared. D, He, C are chosen to be incident particles with an incident angle of 45° [5]. The impact energy varies from 100 eV to 10000 eV. Tungsten

sputtering yields calculated by SDTRIM.SP are shown in figure 6(a). The Li-C coating can dramatically reduce the tungsten sputtering yields and thus protect tungsten from strong erosion; however, the protecting effect is discrepant for different impinging particles. Here we define the relative W sputtering yields as W sputtering yields of the EAST mixed material model divided by the W sputtering yields of the pure W model. The relative W sputtering yields under D, He and C impact is shown in figure 6(b). A 30 Å Li-C coating on the tungsten can reduce the tungsten sputtering yields by two orders of magnitudes, and it is easier for the heavier particles to penetrate through the Li-C enriched layer and cause W erosion. That is, compared with the impinging D and He, the heavier C particles are more effective on tungsten sputtering.

As shown in figure 6(b), for each impact atom species, the relative W sputtering yields increase with the increase of the impact energy. The impact energies of D^+, He^{2+} and C^{6+} corelated to the peak particle flux density of the He discharge during ELMs are also marked in figure 6(b). The impact energy of D^+ is about 5 times of the pedestal electron temperature, which is consistent with previous JET experimental findings [9, 10]. Due to the higher charge state, the C^{6+} gains more energy from both the electric field long the field line and the sheath near the target, thus has an obviously higher impact energy than the main ions. The relative W sputtering yields by the streaming C^{6+} is more than 3 times higher than that caused by D^+ and He^{2+}, which indicates that the Li-C coating will magnify the contribution of the energetic C^{6+} on tungsten erosion. Note that the intra-ELM tungsten erosion profiles have only single peak for both D and He discharges when the pure tungsten model is used, since the tungsten erosion caused by C^{6+} is much lower than that caused by the main ions. The existence of a Li-C overlayer dramatically suppresses the W erosion peak caused by main ions, and thus makes the second peak caused by the C^{6+} more apparent. Therefore, a Li-C coating on EAST divertor (which may not exist on other devices) makes the tungsten erosion caused by C^{6+} prominent and thus makes the double peaks of tungsten erosion significant on EAST.

5. Discussion and conclusions

5.1 Discussion

Previous studies [17] proved that the main ion flux density arriving at the divertor target in the FEM agrees with the FSM when it is assumed that the particles are transported freely at a constant speed of ion's sound speed, but the transport of the impurities remains unknown. In this work, we use the Monte Carlo code to trace the transport of both main ions and impurities (C^{6+}) with a self-consistent electric field from the FEM, and the results are compared with the free streaming particles. As shown in figure 7, for the deuterium discharge 87448, the D particle flux density arriving at the divertor target from the FEM is in a good agreement with the free streaming model with a constant ion's sound speed at the pedestal top. However, for the C^{6+} particles, there exists a big discrepancy between the FEM and the free streaming transport model, which means we cannot simply assume the impurity transport with the sound speed for the impurity transport calculations during ELMs.

Meanwhile, as shown in figure 7, the time delay between the main ions and the impurities (C^{6+}) from the FEM is much longer than the free streaming cases. During ELMs, the existence of the electric field (E) will accelerate the ions to a higher speed, but since the electric field (equation (3)) changes with time and space, the electric filed has different effects on acceleration for main ions and impurities. The C^{6+} impurities have a lower initial thermal speed than D^+, therefore they will spend more time at the upstream region where E is small (x is small), and since E decays with time, the acceleration of the C^{6+} is lower than D^+ all the way to the divertor target, thus reinforcing the C^{6+} even slower.

The time delay between the intra-ELM double W erosion peaks is affected by both the impinging elements and the pedestal parameters. To decouple the incident element effects from the pedestal plasma conditions, we analyzed the double-peaked profiles across a series of H-mode conditions for D plasma discharges. These selected discharges have the same plasma current (I_p = 600 kA) but different electron temperature at the pedestal top (see table A1 in the annex section). As shown in figure 8, the time delay of the double peaks (dt) shows a positive correlation with T_{e_ped}.

To understand this unique correlation, the ELM transport modeling described in section 3 is applied dedicatedly for the selected discharges in table A1. The time delay of the streaming D^+ and C^{6+} derived from the Monte Carlo modeling is in a good agreement with the experimental data, as shown in figure 8. The magnetic connection length from the OMP to the outer divertor target (L) during ELMs is also obtained from the modeling. As listed in table A1, the intra-ELM magnetic connection length L is found to be much longer than the unperturbed inter-ELM value (L_{inter}), which is in consistent with the previous experimental and modeling findings in [10, 34, 35]. Meanwhile, L increases from 110 m to about 220 m with the increase of T_{e_ped} within these discharges. Although a higher T_{e_ped} helps to get a higher transport speed of streaming ions, a longer L dominates that dt *is* in a positive correlation with T_{e_ped}.

In addition to the streaming energetic particles, the intra-ELM W erosion process is also dramatically affected by the thickness of the Li-C overlayer. The relative W sputtering yields for each element (the stars in figure 6(b)) is calculated by adjusting the thickness of the Li-C layer in the mixed material model described in section 4. As shown in figure 9, for all the three impinging elements (D, He and C), the relative W sputtering yields drop quickly as the Li-C thickness increases, which means the intra-ELM W erosion is sensitive to the thickness of the Li-C layer. Previous EAST experimental results also reveal that the divertor tungsten erosion rate is reduced by orders of magnitudes with the Li injection in process during the discharge [27]. Compared with the D and He impinging, the relative W sputtering yields of C impinging drops slower as the Li-C layer getting thicker, indicating that the existence of the Li-C coating will make the contribution from C impinging comparatively more important.

Lithium coating of the EAST first wall significantly reduces the divertor tungsten

erosion [20, 32]. However, the existence of lithium on the tungsten divertor surface makes the material environment too complicated to precisely reproduce the tungsten erosion process by modeling. Previous post mortem analysis proves that there exist large amount of Li and C on the first wall material of EAST [29-31], but still cannot represent the real-time material compositions during the discharges. The erosion and redeposition of the Li and C can change the thickness of the Li-C overlayer during each discharge. Meanwhile, the variation of the Li-C thickness will affect the intra-ELM W erosion profile and thus determine the appearance of the W erosion double-peaks. In some EAST discharges, we find the double-peaks phenomenon appears only in part of the ELMs, which may be caused by the variation of the Li-C layer thickness during the discharge. The Li-C-W mixed material model described in this paper is still an ad hoc model for intra-ELM tungsten erosion calculations in EAST. The precise thickness of the Li-C coating and the material fractions may change in each discharge. The change of material fractions will change the W erosion rate [36], but these information cannot be obtained by present diagnostics. To further evaluate the mixed-material evolution during the discharge, dynamic TRIDYN simulation [37] as well as more advanced in-situ real-time diagnostics are needed.

Note that when calculating the ions' impact energy (equation (7)), a sheath potential of $3T_e$ is assumed, but depending on the secondary electron emission, the sheath potential may change especially during ELMs. However, the impact energy of impinging ions is dominated by the kinetic energy gained during the transport, while the energy gained from the sheath potential contribute less than 25% of the total impact energy for both main ions and impurities. Meanwhile, the W sputtering yields (as shown in figure 6(a)) will not change by more than 20% if the impact energy of ions changes by 25%. Therefore, the variation of the sheath potential will not change the main conclusion of this paper.

Also note that the S/XB coefficient we used in this paper depends on the T_e only. Recent experimental data suggests that the S/XB coefficient also depends on n_e [11], but the experimental data is quite limited and the update of the ADAS database is still ongoing. Therefore, the original S/XB function has been used as well as in many published papers [3, 4, 9, 32, 38-40]. For both the old and the new S/XB models, the double peaks of the intra-ELM W erosion exist on EAST.

5.2 Summary and conclusions

In this paper, the double peaks of intra-ELM tungsten erosion on EAST is reported. To study this unique phenomenon, the ELM parallel transport and the divertor material erosion process are modeled for both D and He discharges.

The plasma free expansion model is employed to simulate the parallel ELM transport from the OMP to the strike point on the divertor target. During ELM transport, a self-consistent electric field is established to ensure the quasi-neutral approximation. Under this electric field, the kinetic energy of electrons will be transferred to ions thus

accelerate the ions to a higher speed. A semi-analytic one-dimensional Monte Carlo tracing code is developed to dedicatedly model the particle transport during ELMs, and modeling results reveal that the C^{6+} particles transport slower than the main ions due to their lower initial thermal speed.

Based on the particle flux density and energy obtained from the Monte Carlo modeling, a Li-C-W mixed-material model is developed to calculate the intra-ELM tungsten erosion rate. A Li-C overlayer will dramatically reduce the tungsten erosion, meanwhile, it can make the heavier impurity comparatively more effective than the main ions on causing tungsten erosion. By adjusting the thickness of the Li-C enriched layer, the tungsten gross erosion rates are well reproduced for both D and He discharges. Modeling results suggest that the second tungsten erosion peak during ELMs is caused by the energetic C^{6+}. As for the main ions, He is proved to be much more effective than the D on causing tungsten erosion, thus more attention should be addressed on He discharge in the future. The key physics governing the intra-ELM tungsten erosion in EAST has been revealed by the interpretive modeling.

Acknowledgements

The work was supported by the National Natural Science Foundation of China under Contract Nos. 12022511, 12005143 and 11861131010, National Key Research and Development Program of China under contract Nos. 2017YFE0301300 and 2017YFA0402500, Postdoctoral Science Foundation of China under contract No. 2020M672764, the Key Research Program of Frontier Sciences, CAS with Grant No. ZDBS-LY-SLH010, the National MCF Energy R&D Program of China under contract No. 2019YFE03080100, the CASHIPS Director's Fund with Grant No. BJPY2019B01 and the Shenzhen Clean Energy Research Institute.

References

[1] K. Krieger, H. Maier, R. Neu, et al 1999 Conclusions about the use of tungsten in the divertor of ASDEX Upgrade Journal of nuclear materials 266 207-216

[2] A. Thoma, K. Asmussen, R. Dux, et al 1997 Spectroscopic measurements of tungsten erosion in the ASDEX Upgrade divertor Plasma physics and controlled fusion 39 1487

[3] R. Ding, P.C. Stangeby, D.L. Rudakov, et al 2015 Simulation of gross and net erosion of high-Z materials in the DIII-D divertor Nuclear Fusion 56 016021

[4] R. Ding, D.L. Rudakov, P.C. Stangeby, et al 2017 Advances in understanding of high-Z material erosion and re-deposition in low-Z wall environment in DIII-D Nuclear Fusion 57 056016

[5] T. Abrams, R. Ding, H.Y. Guo, et al 2017 The inter-ELM tungsten erosion profile in DIII-D H-mode discharges and benchmarking with ERO+ OEDGE modeling Nuclear Fusion 57 056034

[6] S. Brezinsek, J.-E. contributors 2015 Plasma-surface interaction in the Be/W environment: conclusions drawn from the JET-ILW for ITER Journal of nuclear materials 463 11-21

[7] G.L. Xu, J. Guterl, T. Abrams, et al 2019 Modeling of inter-and intra-edge-localized mode tungsten erosion during DIII-D H-mode discharges Nuclear Fusion 59 126018

[8] G.L. Xu, J. Guterl, T. Abrams, et al 2019 Study of DIII-D tungsten erosion processes by using a carbon–

tungsten mixed material model Nuclear Materials and Energy 18 141-146
[9] C. Guillemaut, A. Jardin, J. Horacek, et al 2015 Ion target impact energy during Type I edge localized modes in JET ITER-like wall Plasma Physics and Controlled Fusion 57 085006
[10] C. Guillemaut, C. Metzger, D. Moulton, et al 2018 Experimental validation of an analytical kinetic model for edge-localized modes in JET-ITER-like wall Nuclear Fusion 58 066006
[11] T. Abrams, E.A. Unterberg, A.G. McLean, et al 2018 Experimental validation of a model for particle recycling and tungsten erosion during ELMs in the DIII-D divertor Nuclear Materials and Energy 17 164-173
[12] W. Fundamenski, R.A. Pitts 2005 A model of ELM filament energy evolution due to parallel losses Plasma Physics and Controlled Fusion 48 109
[13] G. Manfredi, S. Hirstoaga, S. Devaux 2010 Vlasov modelling of parallel transport in a tokamak scrape-off layer Plasma Physics and Controlled Fusion 53 015012
[14] T. Eich, A. Kallenbach, W. Fundamenski, et al 2009 On the asymmetries of ELM divertor power deposition in JET and ASDEX Upgrade Journal of nuclear materials 390 760-763
[15] V.F. Kovalev, V.Y. Bychenkov, V.T. Tikhonchuk 2002 Particle dynamics during adiabatic expansion of a plasma bunch Journal of Experimental and Theoretical Physics 95 226-241
[16] D.S. Dorozhkina, V.E. Semenov 1998 Exact solution of Vlasov equations for quasineutral expansion of plasma bunch into vacuum Physical review letters 81 2691
[17] D. Moulton, P. Ghendrih, W. Fundamenski, et al 2013 Quasineutral plasma expansion into infinite vacuum as a model for parallel ELM transport Plasma Physics and Controlled Fusion 55 085003
[18] A. Mutzke, G. Bandelow, R. Schneider 2015 Sputtering of mixed materials of beryllium and tungsten by hydrogen and helium Journal of Nuclear Materials 467 413-417
[19] B. Zhang, X. Gong, J. Qian, et al 2020 H-mode operation in helium plasma with tungsten divertor and low input torque in EAST Nuclear Fusion
[20] F. Ding, G.-N. Luo, X. Chen, et al 2019 Plasma–tungsten interactions in experimental advanced superconducting tokamak (EAST) Tungsten 1-10
[21] T. Ming, W. Zhang, J. Chang, et al 2009 Improvement of divertor triple probe system and its measurements under full graphite wall on EAST Fusion engineering and design 84 57-63
[22] Z. Xu, Z.W. Wu, W. Gao, et al 2016 Filterscope diagnostic system on the experimental advanced superconducting tokamak (EAST) Review of Scientific Instruments 87 11D429
[23] Q. Zang, J. Zhao, L. Yang, et al 2011 Upgraded multipulse laser and multipoint Thomson scattering diagnostics on EAST Review of Scientific Instruments 82 063502
[24] S. Brezinsek, A. Kirschner, M. Mayer, et al 2019 Erosion, screening, and migration of tungsten in the JET divertor Nuclear fusion 59 096035
[25] M. Laengner, S. Brezinsek, J.W. Coenen, et al 2013 Penetration depths of injected/sputtered tungsten in the plasma edge layer of TEXTOR Journal of Nuclear Materials 438 S865-S870
[26] G.Z. Zuo, J.S. Hu, J.G. Li, et al 2013 Lithium coating for H-mode and high performance plasmas on EAST in ASIPP Journal of Nuclear Materials 438 S90-S95
[27] W. Xu, J.S. Hu, R. Maingi, et al 2018 Real-time reduction of tungsten impurity influx using lithium powder injection in EAST Fusion Engineering and Design 137 202-208
[28] W. Eckstein, Computer simulation of ion-solid interactions, Springer Science & Business Media2013.
[29] R. Yan, J. Peng, R. Ding, et al 2019 Surface Recovery of the CXRS First Mirror of EAST IEEE Transactions on Plasma Science 47 1769-1773
[30] C. Li, Y. Wang, X. Wu, et al 2017 Compositions and chemical states on the co-deposition layer of

lithiated tungsten of plasma-facing components of EAST Nuclear Materials and Energy 12 1209-1213
[31] C. Li, D. Zhao, Z. Hu, et al 2015 Characterization of deuterium retention and co-deposition of fuel with lithium on the divertor tile of EAST using laser induced breakdown spectroscopy Journal of Nuclear Materials 463 915-918
[32] H. Mao, F. Ding, G.-N. Luo, et al 2017 The impacts of lithium and silicon coating on the W source in EAST Nuclear Materials and Energy 12 447-452
[33] H. Xie, R. Ding, A. Kirschner, et al 2017 ERO modelling of tungsten erosion and re-deposition in EAST L mode discharges Physics of Plasmas 24 092512
[34] G.T.A. Huysmans, S. Pamela, E. Van Der Plas, et al 2009 Non-linear MHD simulations of edge localized modes (ELMs) Plasma Physics and Controlled Fusion 51 124012
[35] S. Pamela, T. Eich, L. Frassinetti, et al 2015 Non-linear MHD simulations of ELMs in JET and quantitative comparisons to experiments Plasma Physics and Controlled Fusion 58 014026
[36] W. Eckstein, J. Roth 1991 Sputtering of tungsten by carbon Nuclear Instruments and Methods in Physics Research Section B: Beam Interactions with Materials and Atoms 53 279-284
[37] W. Möller, W. Eckstein 1984 Tridyn—A TRIM simulation code including dynamic composition changes Nuclear Instruments and Methods in Physics Research Section B: Beam Interactions with Materials and Atoms 2 814-818
[38] G.J. Van Rooij, J.W. Coenen, L. Aho-Mantila, et al 2013 Tungsten divertor erosion in all metal devices: Lessons from the ITER like wall of JET Journal of Nuclear Materials 438 S42-S47
[39] N. Den Harder, S. Brezinsek, T. Pütterich, et al 2016 ELM-resolved divertor erosion in the JET ITER-like wall Nuclear fusion 56 026014
[40] A. Kirschner, S. Brezinsek, A. Huber, et al 2019 Modelling of tungsten erosion and deposition in the divertor of JET-ILW in comparison to experimental findings Nuclear materials and energy 18 239-244

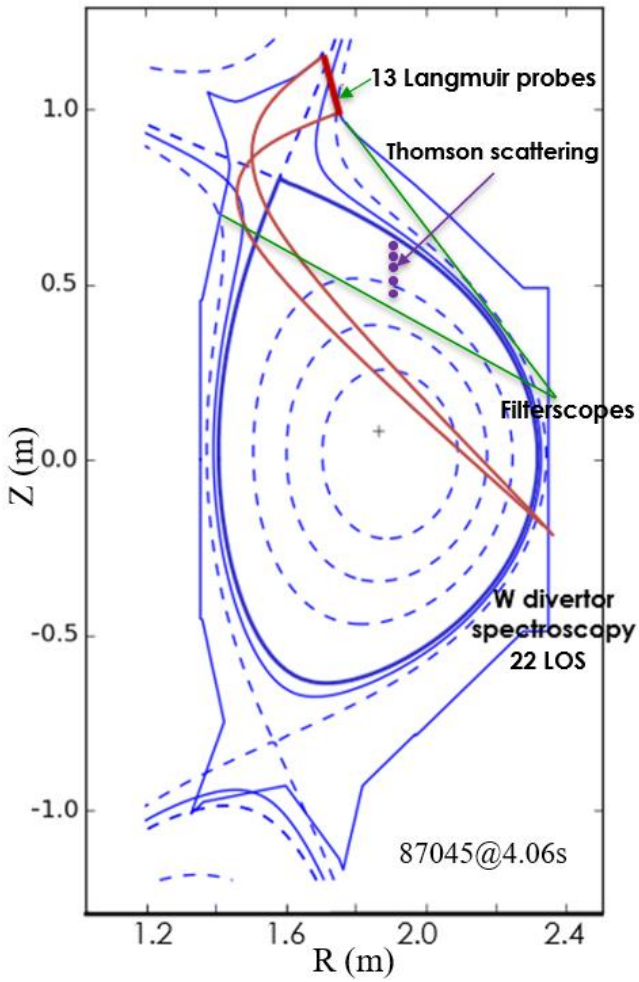

Figure 1. The cross section of the EAST main chamber with sight lines of the spectroscopic diagnostics discussed in this paper, overlaid on the magnetic equilibrium of discharge 87045 at 4.06 s.

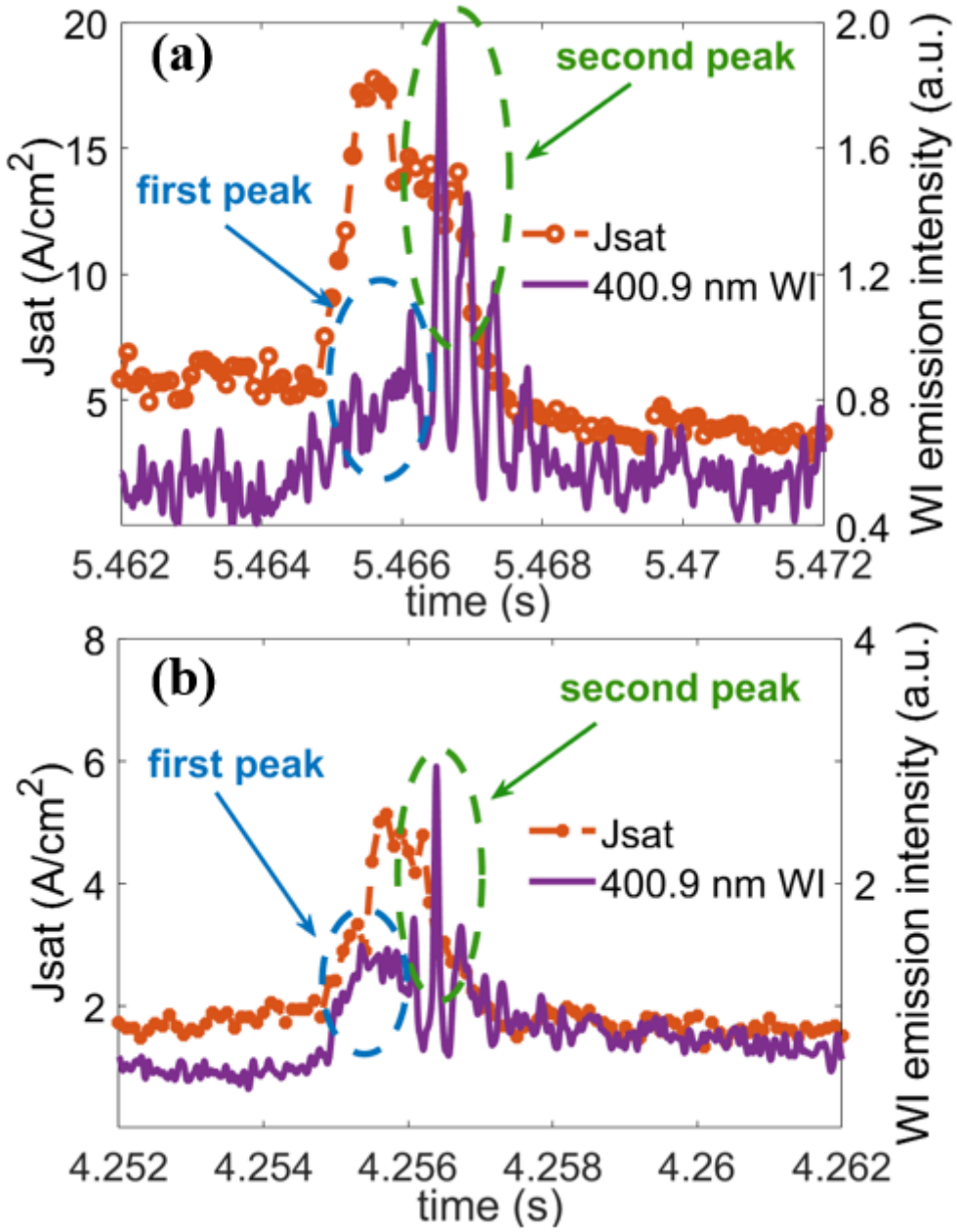

Figure 2. The ion saturation current (averaged every 100 μs) and the 400.9 nm WI emission intensity at the strike point of the upper outer divertor target for (a) deuterium discharge 87448, and (b) helium discharge 87045. Double peaks of W erosion are observed during ELM burst.

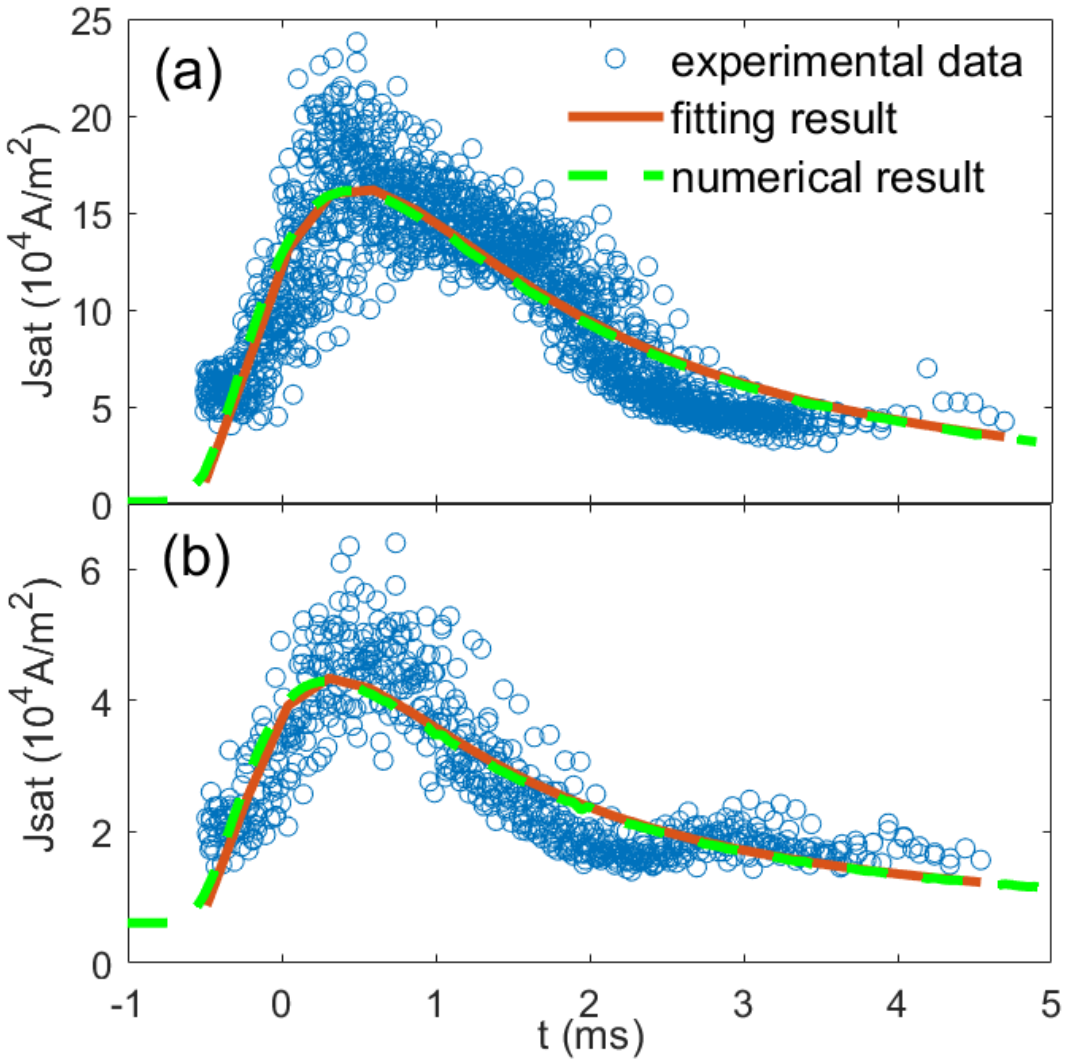

Figure 3. The best fitting results of ion saturation current on the strike point by using equation (2) and the numerical results from the Monte Carlo tracing code (shifted by a δt). (a) D discharge 87448, (b) He discharge 87045. Circles are the Langmuir probe data, red lines are the fitting results, and the green-dash lines are the numerical results.

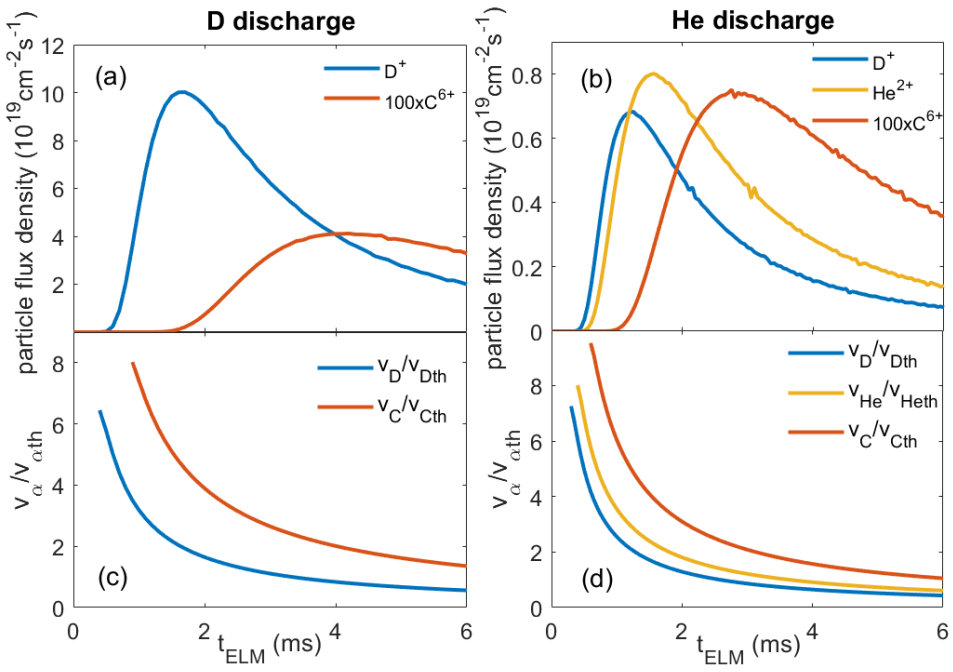

Figure 4. Particle flux density and normalized average velocity of streaming particles at the divertor target after the ELM burst at the OMP for the D (a, c) and He (b, d) discharges respectively. Blue lines refer to D^+, yellow lines refer to He^{2+}, and red lines refer to C^{6+}. The initial C^{6+} concentration is assumed to be 1% and the C^{6+} flux density is multiplied by 100 for a better comparison.

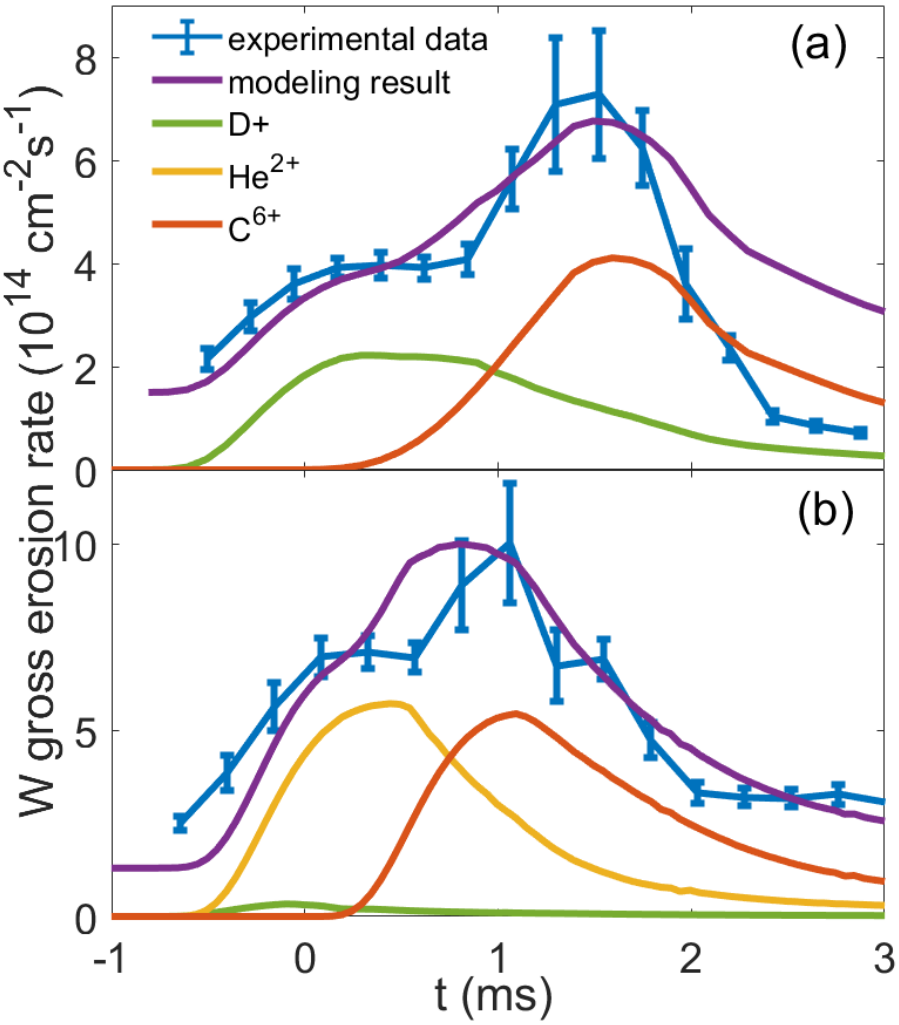

Figure 5. Intra-ELM tungsten gross erosion rate for (a) D discharge 87448 and (b) He discharge 87045. The blue lines are the experimental data. The violet lines are the total W erosion rates from the modeling results. The green, yellow and red lines represent the W erosion caused by the impinging D^+, He^{2+} and C^{6+} accordingly.

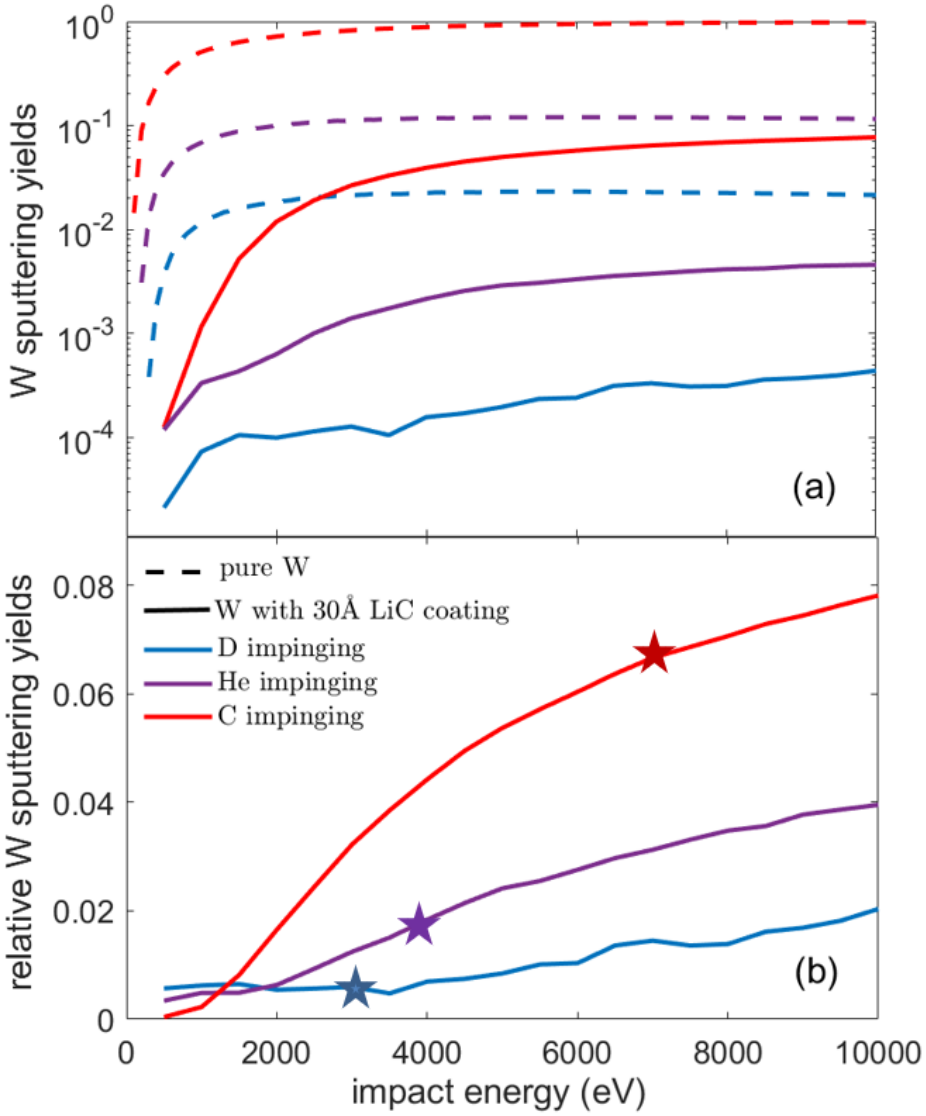

Figure 6. W sputtering yields calculated by SDTRIM.SP. (a) W sputtering yields of pure tungsten (dashed lines) and 30 Å Li-C coating tungsten (solid lines) impacted by D (blue lines), He (violet liens) and C (red lines). (b) Relative W sputtering yields under D (blue line), He (violet line) and C (red line) impinging. Stars in (b) represent the average impact energy of D (blue star), He (violet star) and C (red star) during ELMs of the selected He discharge.

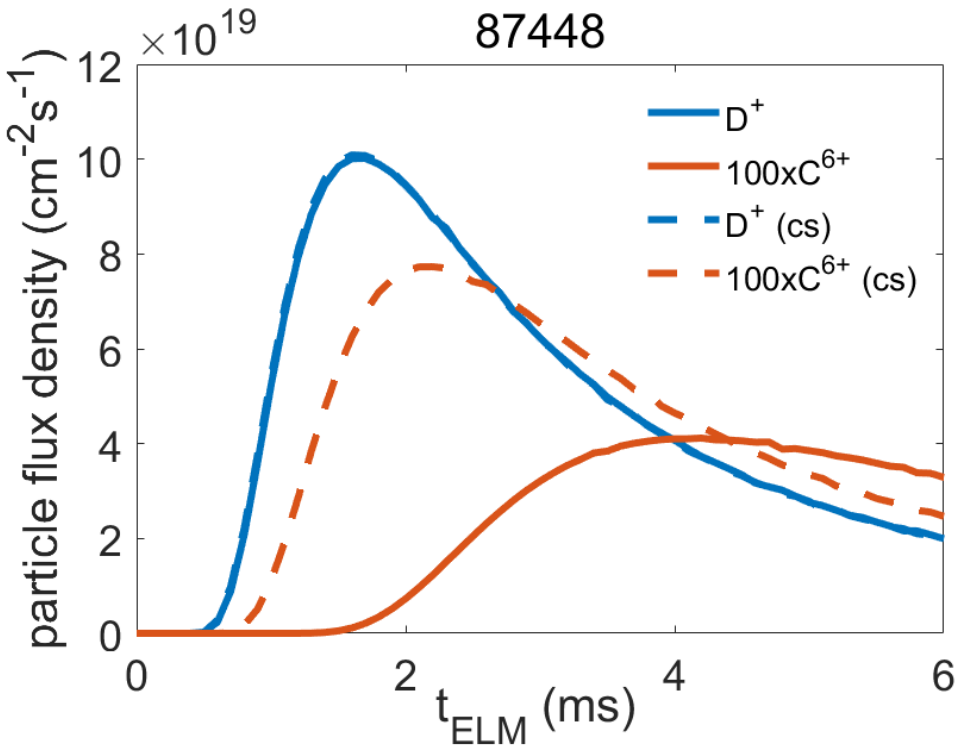

Figure 7, Particle flux densities arriving at the divertor target derived from the Monte Carlo simulations. Blue lines are the D^+ particles and red lines are the C^{6+} particles multiplied by 100. Solid lines are the particle transport result with existence of the electric field (FEM). Dashed lines are the particle transport result with constant speed of ion's sound speed.

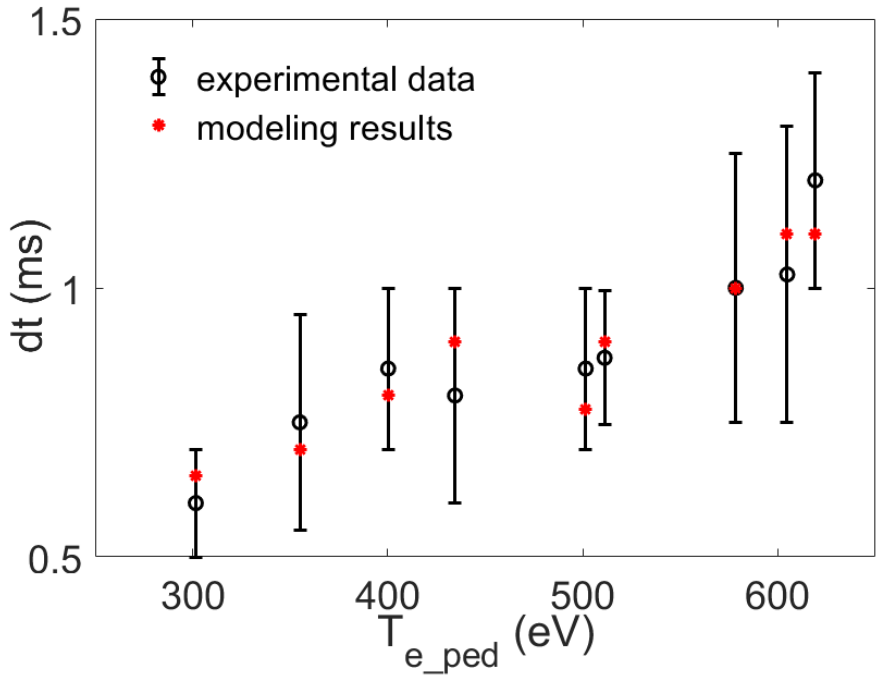

Figure 8. The time delay between the intra-ELM double W erosion peaks for different discharges with pedestal top electron temperature varying from 300 eV to 620 eV. Red stars are the time delay between the peak particle flux density of the streaming D^{+} and C^{6+} derived from the modeling.

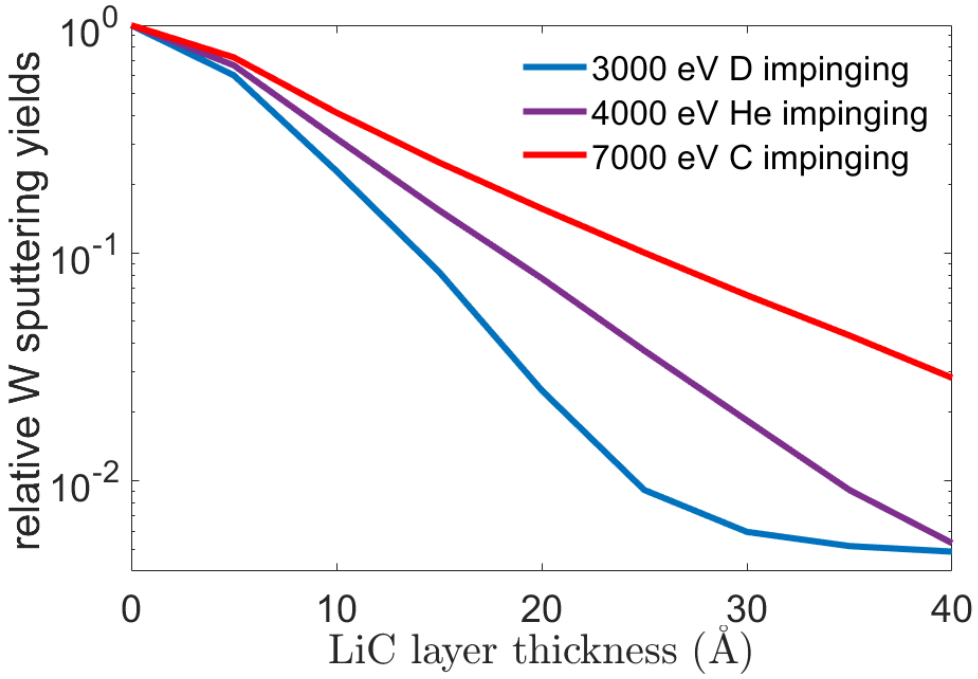

Figure 9. Relative W sputtering yields of W coated by different thickness of Li-C layer, under D (blue line), He (violet line) and C (red line) impinging.

Annex

Table A1. Main plasma parameters, magnetic connection lengths and the measured time delay between erosion peaks of the selected discharges

shot NO.	T_{e_ped} *(eV)*	n_{e_ped} $(10^{19}m^{-3})$	I_p (kA)	P_{heat} *(MW)*	f_{ELM} *(Hz)*	L *(m)*	L_{inter} *(m)*	L/L_{inter}	dt *(ms)*
71439	501.5	3.00	600	10.8	85	170	28.2	6.03	0.850
71443	619.2	2.23	600	6.5	80	214	28.1	7.61	1.200
71444	400.2	2.65	600	4.5	60	149	26.5	5.61	0.850
71445	604.8	1.98	600	7.0	65	224	27.8	8.05	1.025
71447	578.4	2.34	600	8.8	80	204	27.4	7.43	1.000
71448	434.5	2.08	600	8.8	140	163	27.6	5.91	0.800
71449	511.2	1.73	600	6.3	110	173	27.3	6.34	0.870
71451	301.6	2.25	600	3.0	60	110	27.7	3.97	0.600
71456	354.9	3.02	600	4.2	45	134	27.8	4.83	0.700